ACS APPLIED MATERIALS & INTERFACES

Research Article

www.acsami.org

Conjugation of Iron Oxide Nanoparticles with RGD-Modified Dendrimers for Targeted Tumor MR Imaging

Jia Yang,[†,‡,∥] Yu Luo,[§,∥] Yanhong Xu,[†,∥] Jingchao Li,[§] Zaixian Zhang,[†] Han Wang,[†] Mingwu Shen,[§] Xiangyang Shi,*[,§] and Guixiang Zhang*[,†]

[†]Department of Radiology, Shanghai First People's Hospital, School of Medicine, Shanghai Jiaotong University, Shanghai 200080, P. R. China

[‡]Department of Radiology, Shanghai Songjiang Central Hospital, Shanghai 201699, P.R. China

[§]College of Chemistry, Chemical Engineering and Biotechnology, Donghua University, Shanghai 201620, P. R. China

S *Supporting Information*

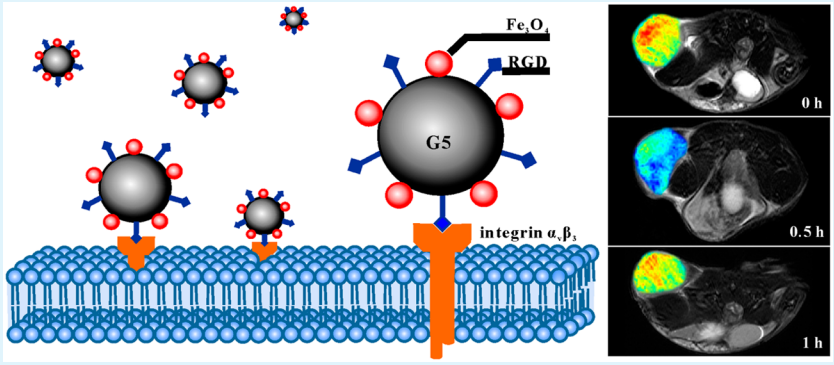

ABSTRACT: This article reports a new approach for the synthesis of ultrasmall iron oxide nanoparticles (NPs) conjugated with Arg-Gly-Asp (RGD)-modified dendrimers (G5.NHAc-RGD-Fe_3O_4 NPs) as a platform for targeted magnetic resonance (MR) imaging of C6 glioma cells. Ultrasmall Fe_3O_4 NPs synthesized via a solvothermal route were conjugated with RGD peptide-modified generation-5 poly(amidoamine) dendrimers (G5.NH_2-RGD). The final G5.NHAc-RGD-Fe_3O_4 NPs were formed following the acetylation of the remaining dendrimer terminal amines. The as-prepared multifunctional Fe_3O_4 NPs were characterized using various techniques. The results of a cell viability assay, cell morphological observation, and hemolysis assay indicated that the G5.NHAc-RGD-Fe_3O_4 NPs exhibit excellent cytocompatibility and hemocompatibility over the studied concentration range. In addition, RGD conjugated onto the Fe_3O_4 NPs allows for the efficient targeting of the particles to C6 cells that overexpress $\alpha_v\beta_3$ receptors, which was confirmed via *in vitro* cell MR imaging and cellular uptake. Finally, the G5.NHAc-RGD-Fe_3O_4 NPs were used in the targeted MR imaging of C6 glioma cells in mice. The results obtained from the current study indicate that the developed G5.NHAc-RGD-Fe_3O_4 NPs offer significant potential for use as contrast agents in the targeted MR imaging of different types of tumors.

KEYWORDS: *ultrasmall iron oxide nanoparticles, dendrimer, RGD, MR imaging, cancer cells*

INTRODUCTION

Recently, molecular imaging techniques have been widely developed for the diagnosis and detection of early stage tumors.[1−4] Among the current imaging modes, magnetic resonance (MR) imaging is a useful and noninvasive modality because of its high tomographic capabilities,[5,6] long effective imaging windows,[7−9] and high resolution and accuracy.[10−12] To improve the imaging sensitivity, selected contrast agents are important in clinical trials. Recent advances in nanotechnology have made it possible to use nanoparticles (NPs) as contrast agents for MR imaging. For example, Gd(III)- or Mn(II)-based NPs can be used for T_1-weighted MR imaging,[13−15] and superparamagnetic iron oxide (Fe_3O_4) NPs can be employed as negative contrast agents for T_2-weighted MR imaging applications.[16−19] Because of their unique magnetic properties, high sensitivity, and low toxicity, superparamagnetic Fe_3O_4 NPs have advantages over Gd(III)- or Mn(II)-based NPs as contrast agents for MR imaging.[20,21]

However, superparamagnetic Fe_3O_4 NPs tend to aggregate and show a decrease in dissolution rates, especially if they are exposed to biological fluids or magnetic fields.[22,23] Therefore, appropriate surface modifications or coatings are necessary to improve the water dispersity, colloidal stability, and biocompatibility of Fe_3O_4 NPs. Various polymers or small-molecule-

Received: December 22, 2014
Accepted: February 19, 2015
Published: February 19, 2015

DOI: 10.1021/am508983n
ACS Appl. Mater. Interfaces 2015, 7, 5420−5428

coated Fe_3O_4 NPs have been reported for different biomedical applications.[24]

Another issue associated with the use of Fe_3O_4 NPs in tumor diagnosis is the lack of ability to target tumor sites. A targeting strategy could reduce the side effects of the particles on normal cells but increase their uptake by cancer cells. Therefore, it would be advantageous to construct Fe_3O_4 NPs with specific targeting abilities after modification with certain ligands that can recognize molecular signatures on the surface of cancer cells, e.g., peptides,[25−28] folic acid (FA),[2,29,30] antibodies,[31,32] galactose,[33,34] chlorotoxin,[35,36] and hyaluronic acid (HA).[37−39]

In a previous study, ultrasmall Fe_3O_4 NPs were successfully synthesized via a simple one-pot solvothermal method using trisodium citrate as a crystal grain growth inhibitor and stabilizer.[40] The as-synthesized Fe_3O_4 NPs, which exhibited a range of sizes, not only showed excellent colloidal stability and good biocompatibility but also displayed significant potential for use as T_1 contrast agents.

In this study, ultrasmall Fe_3O_4 NPs synthesized via the above-described method (Fe_3O_4-COOH NPs) were further conjugated with Arg-Gly-Asp (RGD)-modified generation-5 poly(amidoamine) dendrimers (G5.NH_2-RGD). Following acetylation, ultrasmall Fe_3O_4 NPs conjugated with RGD-modified dendrimers (G5.NHAc-RGD-Fe_3O_4 NPs) were formed. The products were characterized using various techniques, and the G5.NHAc-RGD-Fe_3O_4 NPs showed good water dispersibility, colloidal stability, and excellent hemocompatibility and biocompatibility over the studied concentration range. *In vitro* cellular uptake analysis suggested that G5.NHAc-RGD-Fe_3O_4 NPs have a higher binding affinity toward C6 cells that overexpress $\alpha_v\beta_3$ receptors than G5.NH.Ac-Fe_3O_4 NPs. *In vitro* cell and *in vivo* tumor MR imaging experiments not only indicated good T_2-weighted MR imaging performance but also demonstrated the specific targeting ability of G5.NHAc-RGD-Fe_3O_4 NPs to C6 cells; therefore, these nanoparticles can be used for targeted MR imaging of tumors via the RGD-mediated pathway.

EXPERIMENTAL SECTION

Materials. Ethylenediamine core G5.NH2 PAMAM dendrimers with a polydispersity index less than 1.08 were purchased from Dendritech (Midland, MI, USA). The cyclic RGD peptide (M_w = 706.8) was purchased from GenicBio BioTech Co. Ltd. (Shanghai, China). Oleylamine, 1-ethyl-3-[3-(dimethylamino)propyl] carbodiimide hydrochloride (EDC), and *N*-hydroxysuccinimide (NHS) were supplied by J&K Chemical Ltd. (Shanghai, China). Ferric chloride hexahydrate ($FeCl_3{\cdot}6H_2O$ > 99%), diethylene glycol (DEG), trisodium citrate, triethylamine, acetic anhydride, and all other chemicals and solvents were purchased from Sigma-Aldrich (St. Louis, MO, USA) and used as received. C6 cells (a rat C6 glioma cell line) were obtained from the Institute of Biochemistry and Cell Biology, Chinese Academy of Science (Shanghai, China). RPMI 1640 medium, fetal bovine serum (FBS), penicillin, and streptomycin were obtained from Hangzhou Jinuo Biomedical Technology Co. Ltd., China, and 3-(4,5-dimethylthiazol-2-yl)-2,5-diphenyltetrazolium bromide (MTT) was purchased from Sigma-Aldrich. The water used in all experiments was purified using a Milli-Q Plus 185 water purification system (Millipore, Bedford, MA, USA) and exhibited a resistivity greater than 18.2 MΩ·cm. Regenerated cellulose dialysis membranes (MWCO = 1,000) were acquired from Fisher.

Synthesis of Fe_3O_4-COOH NPs. Anhydrous $FeCl_3$ (2 mmol) was first vigorously mixed with 20 mL of DEG to form a clear solution. Then, Na_3Cit (0.8 mmol) was added, and the mixture was heated to 80 °C with stirring to form a clear solution. After dissolving anhydrous NaOAc (6 mmol) in the previously mentioned solution, the mixture was transferred to a Teflon-lined stainless-steel autoclave (50 mL) and sealed in air. Following this step, the autoclave was held at 200 °C for 4 h. After being naturally cooled to room temperature, the black product was collected by sedimentation with the aid of an external magnetic field and purified with ethanol three times to remove excess reactants and byproducts. The resulting precipitate was dried at 60 °C for further use.

Fabrication of G5.NH_2-RGD. The G5.NH_2-RGD conjugate was synthesized according to our previous report.[15] Briefly, G5.NH_2 (26.00 mg, 10 mL in DMSO) was first activated with 1 mol equiv of *N*-succinimidyl 6-maleimidohexanoate (6 M, 3.08 mg, 2 mL in DMSO) under vigorous magnetic stirring at room temperature for 8 h. Then, RGD (6.92 mg, 2 mL in DMSO) was added, and the ensuing reaction was allowed to proceed for 12 h, yielding a raw product of G5.NH_2-RGD. The DMSO and excess reactants and byproducts were removed from the mixture via extensive dialysis against PBS (three times, 2 L) and water (six times, 2 L) for 3 d, followed by lyophilization to obtain G5.NH_2-RGD.

Synthesis of G5.NHAc-RGD-Fe_3O_4 NPs. The carboxyl groups of Fe_3O_4-COOH NPs (56 mg, 15 mL HEPES buffer solution) were activated with EDC (144 mg) and NHS (70 mg) in MES buffer solution. Then, the activated Fe_3O_4-COOH NPs were added dropwise into the solution of G5.NH_2-RGD (1 μmol, 15 mL of MES buffer solution), and the mixture was stirred for 3 d. The remaining amino groups on the G5.NH_2-RGD-Fe_3O_4 NPs were further acetylated to reduce their surface potentials. Briefly, 287 μL of triethylamine was added to the G5.NH_2-RGD-Fe_3O_4 NPs aqueous solution, and the solution was thoroughly mixed for 30 min. Then, 146 μL of acetic anhydride was added dropwise into the above-mentioned solution under vigorous magnetic stirring at room temperature, and the reaction was allowed to proceed for 24 h. After being centrifuged and washed with water (at least three times), the G5.NHAc-RGD-Fe_3O_4 NPs were finally obtained and dispersed in 10 mL of water. As a control, G5.NHAc-Fe_3O_4 NPs were also prepared using a similar route.

Characterization Techniques. ^{1}H NMR spectra were collected on a Bruker AV400 nuclear magnetic resonance spectrometer in DMSO-d_6. MALDI-TOF mass spectra were acquired using a 4800 Plus MALDI TOF/TOFTM Analyzer (AB SCIEX, Framingham, MA) in linear mode. Thermogravimetric analysis (TGA) was performed using a TG 209 F1 (NETZSCH Instruments Co., Ltd., Germany) thermogravimetric analyzer, and the samples were heated from room temperature to 700 °C at a rate of 20 °C/min under nitrogen gas. The zeta potentials and hydrodynamic sizes of the particles were measured with a Malvern Zetasizer Nano ZS model ZEN3600 (Worcestershire, U.K.) equipped with a standard 633 nm laser. The sizes and morphologies of the particles were characterized using transmission electron microscopy (TEM, 200 kV, JEOL 2010F, Japan); the TEM sample was prepared by transferring one drop of solution onto a carbon-coated copper grid, which was left undisturbed until it had dried. The Fe concentration in all experiments was analyzed using a Leeman Prodigy Inductively Coupled Plasma-Atomic Emission Spectroscopy (ICP-AES) system (Hudson, NH03051, USA). T_2 relaxometry measurements and T_2-weighted MR imaging were performed using an NMI20-Analyst NMR Analyzing and Imaging system (Shanghai Niumag Corporation). The samples were diluted with distilled water to different Fe concentrations, and the instrumental parameters were a magnetic field strength of 0.5 T, point resolution = 156 mm × 156 mm, section thickness = 0.6 mm, TR = 4000 ms, TE = 60 ms, and number of excitations = 1.

Hemolysis Assay. Fresh human blood stabilized with EDTA was kindly provided by Shanghai First People's Hospital (Shanghai, China). The fresh human blood was centrifuged to remove the serum, and the resulting human red blood cells (HRBCs) were purified by five successive repetitions of rinsing with PBS. After 10-fold dilution of the HRBC in PBS, aliquots of the HRBC suspension (0.1 mL) were added into Eppendorf tubes containing 0.9 mL of water (positive control), 0.9 mL of PBS (negative control), or 0.9 mL of PBS containing G5.NHAc-RGD-Fe_3O_4 NPs at different Fe concentrations (5−100 μg/mL). The mixtures were vortexed and held still for 2 h at

DOI: 10.1021/am508983n
ACS Appl. Mater. Interfaces 2015, 7, 5420−5428

room temperature. The samples were then centrifuged (10000 rpm, 1 min), photographs of the samples were taken, and the absorbance of the supernatants (hemoglobin) were collected using a PerkinElmer Lambda 25 UV−vis spectrometer. The hemolysis percentages of the different samples were calculated by dividing the difference in the absorbances between the samples and the negative control by the difference in absorbance between the positive and negative controls.

Cytotoxicity Assay and Cell Morphology Observation. C6 cells were continuously cultured in 25 cm^2 plates in regular RPMI 1640 medium supplemented with 10% heat-inactivated fetal bovine serum (FBS), penicillin (100 U/mL), and streptomycin (100 μg/mL) at 37 °C and 5% CO_2. The cytotoxicity evaluations were performed using a standard MTT assay. Briefly, C6 cells at an initial density of 1 × 10^4 cells per well were seeded into a 96-well plate in 200 μL of RPMI 1640 medium. After incubation for 12 h, the medium was replaced with 200 μL of fresh medium containing pure PBS (control), G5.NHAc-RGD-Fe_3O_4 NPs, or G5.NHAc-Fe_3O_4 NPs at different Fe concentrations (5, 10, 25, 50, and 100 μg/mL). The MTT solution (20 μL, 5 mg/mL in PBS) was added into each well to detect metabolically active cells after incubation at 37 °C and 5% CO_2 for 24 h. The cells were further incubated at 37 °C for another 4 h, and 200 μL of DMSO was added to each well to replace the culture medium. After dissolving the insoluble formazan crystals by mildly shaking the plate for 15 min, the absorbance of each well was measured using a Thermo Scientific Multiskan MK3 ELISA reader (Thermo Scientific, USA) at 570 nm. Each absorbance measurement was performed five times to calculate the mean and standard deviation.

The cell morphologies were also observed via phase contrast microscopy (Leica DM IL LED inverted phase contrast microscope) after the C6 cells were treated with PBS, G5.NHAc-RGD-Fe_3O_4 NPs, or G5.NHAc-Fe_3O_4 NPs at different Fe concentrations (5, 10, 25, 50, and 100 μg/mL) for 24 h. The magnification was set at 200× for each sample.

Cellular Uptake Assay. The cellular uptake of G5.NHAc-RGD-Fe_3O_4 NPs or G5.NHAc-Fe_3O_4 NPs by C6 cells was quantitatively studied using ICP-AES. Briefly, C6 cells were seeded in 12-well plates at an initial density of 5 × 10^5 cells/well with 1 mL of RPMI 1640 medium. After incubation at 37 °C and 5% CO_2 for 12 h, the medium was carefully discarded, and 1 mL of fresh medium containing G5.NHAc-RGD-Fe_3O_4 NPs or G5.NHAc-Fe_3O_4 NPs at different Fe concentrations (5, 10, 25, 50, and 100 μg/mL) was added into each well. After incubation for 4 h, the cells were washed with PBS, harvested, and suspended in 1 mL of PBS. The cells were counted using a hemocytometer. Before the ICP-AES experiments, the cells were dissolved in an aqua regia solution and diluted twice with PBS. Three samples were collected under each condition to obtain the mean and standard deviation. In addition, the cellular uptake of G5.NHAc-RGD-Fe_3O_4 NPs or G5.NHAc-Fe_3O_4 NPs by normal cells (L929 cells) was confirmed using ICP-AES and a method similar to the one described above.

***In Vitro* Targeted Cell MR Imaging.** C6 cells were seeded into 6-well plates at a density of 2 × 10^6 cells per well with 2 mL of RPMI 1640 medium for 12 h. Then, the medium was replaced with 2 mL of fresh medium containing G5.NHAc-RGD-Fe_3O_4 NPs or G5.NHAc-Fe_3O_4 NPs at different Fe concentrations (5, 10, 25, 50, and 100 μg/mL), and the cells were sequentially incubated at 37 °C and 5% CO_2 for 4 h. The cells were then washed with PBS, harvested, and suspended in 1 mL of PBS (containing 0.5% agarose) in 2 mL Eppendorf tubes. T_2 MR imaging of the cell suspensions in each tube was performed using a GE Discovery MR750 3T scanner and an animal coil suitable for mouse imaging (Magtron Inc., Shanghai, China) with a T_2-weighted FSE sequence (slice thickness of 3.4 mm, TR/TE 3000/87.4 ms, 8 × 8 cm FOV, and 320 × 256 matrix).

***In Vivo* Tumor Targeted MR Imaging.** All animal experiments were performed according to protocols approved by the institutional committee for animal care and in accordance with the policy of the National Ministry of Health. Male BALB/c nude mice aged 4 to 6 weeks (15−20 g) were purchased from Shanghai SLAC Laboratory Animal Center (China). To establish the tumor model, 2 × 10^6 C6 cells/mouse were subcutaneously implanted into the left back of the nude mice. The experiments were performed when the xenografted tumor volume reached approximately 0.6 cm^3. The C6 tumor-bearing nude mice were anesthetized by intraperitoneal injection of pentobarbital sodium (40 mg/kg). Subsequently, 0.1 mL of a PBS solution of G5.NHAc-RGD-Fe_3O_4 NPs or G5.NHAc-Fe_3O_4 NPs (600 μg Fe) was delivered into the C6 tumor-bearing nude mice via the tail vein. MR imaging was performed using a GE Discovery MR750 3T scanner with an animal coil suitable for mouse imaging (Magtron Inc., Shanghai, China). The mice were imaged before and after administration of the particles at 0.5, 1, 2, and 4 h. The parameters were 1.8 mm slice thickness, TR/TE 4000/96.6 ms, 3 × 3 cm FOV, and 320 × 256 matrix.

***In Vivo* Biodistribution.** The C6 tumor-bearing nude mice were submitted to *in vivo* biodistribution analysis to understand the metabolic behavior of G5.NHAc-RGD-Fe_3O_4 NPs. The mice were first anesthetized via intraperitoneal injection of pentobarbital sodium (40 mg/kg). Then, 0.1 mL of a PBS solution of G5.NHAc-RGD-Fe_3O_4 NPs or G5.NHAc-Fe_3O_4 NPs (600 μg Fe) was intravenously injected into the C6 tumor-bearing nude mice. At different times, the mice were euthanized, and the main organs, i.e., the heart, liver, spleen, lungs, and kidneys, and the tumor tissue were extracted and weighed. For the ICP-AES measurements, these tissues were subsequently cut into 1−2 mm^2 pieces and digested in aqua regia solutions for 1 d.

RESULTS AND DISCUSSION

Synthesis and Characterization of G5.NHAc-RGD-Fe_3O_4 NPs. In this study, citric acid-stabilized ultrasmall Fe_3O_4-COOH NPs were successfully synthesized according to previous work. RGD-conjugated generation-5 poly(amidoamine) dendrimers (G5.NH_2-RGD) were then used as templates for synthesizing the targeting particles, followed by acetylation of the remaining dendrimer terminal amines (Scheme 1). The resulting G5.NHAc-RGD-Fe_3O_4 NPs were characterized using various techniques.

RGD-conjugated G5.NH_2 was synthesized using 6-maleimidohexanoic acid *N*-hydroxysuccinimide ester as a heterobifunctional cross-linker according to previous work, and the yield of G5.NH_2-RGD was 86.3%. After purification via dialysis, the

Scheme 1. Schematic Representation of the Preparation of the G5.NHAc-RGD-Fe_3O_4 NPs

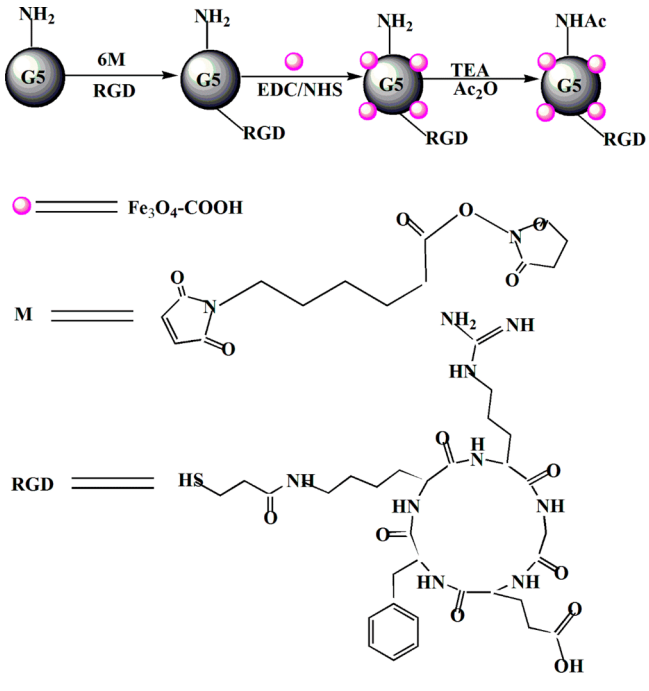

DOI: 10.1021/am508983n
ACS Appl. Mater. Interfaces 2015, 7, 5420−5428

resulting G5.NH_2-RGD was characterized using MALDI-TOF mass spectroscopy (Figure S1, Supporting Information). In the MALDI-TOF mass spectra, the M_w of G5.NH_2 (26095) increased to 27425 after RGD conjugation, suggesting that 2 RGD molecules were coupled to each G5.NH_2.

TGA was performed to analyze the inorganic content of the different particles (Figure 1). The Fe_3O_4-COOH NPs showed a

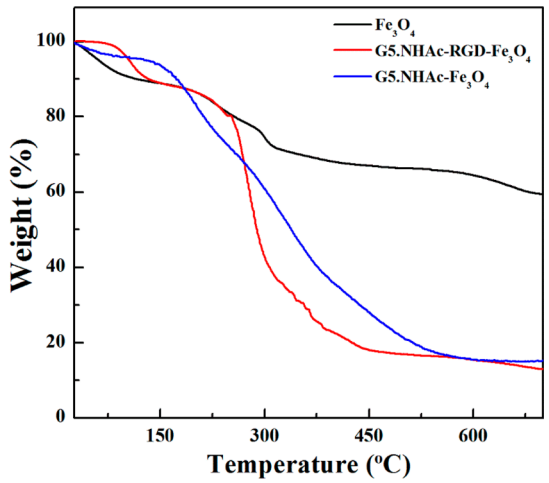

Figure 1. TGA curves of Fe_3O_4-COOH NPs, G5.NHAc-Fe_3O_4 NPs, and G5.NHAc-RGD-Fe_3O_4 NPs.

weight loss of 68.6% due to the citric acid surface coating of the particles. After modification with G5.NH_2 or G5.NH_2-RGD and acetylation, the weight loss was 16.8% for G5.NHAc-RGD-Fe_3O_4 NPs and 16.9% for G5.NHAc-Fe_3O_4 NPs. The reduction in the inorganic content of the particles suggested that the chemical reaction and acetylation were successfully achieved.

Zeta potential measurements and dynamic light scattering (DLS) were employed to confirm the surface charge and hydrodynamic sizes of the different products. As shown in Table 1, Fe_3O_4-COOH NPs, G5.NHAc-Fe_3O_4 NPs, and

Table 1. Zeta Potentials and Hydrodynamic Sizes of Fe_3O_4-COOH, G5.NHAc-Fe_3O_4, and G5.NHAc-RGD-Fe_3O_4 NPs

sample	zeta potential (mV)	hydrodynamic size (nm)
Fe_3O_4-COOH	−43.4	18.6
G5.NHAc-Fe_3O_4	−4.8	453.9
G5.NHAc-RGD-Fe_3O_4	−5.5	527

G5.NHAc-RGD-Fe_3O_4 NPs have surface potentials of −43.4 mV, −4.8 mV, and −5.5 mV, respectively, due to the different functional groups on the surface of the respective particles. The hydrodynamic size results are also shown in Table 1; the hydrodynamic size of the G5.NHAc-Fe_3O_4 NPs (453.9 nm) and G5.NHAc-RGD-Fe_3O_4 NPs (527.0 nm) was much larger than that of the Fe_3O_4-COOH NPs (18.6 nm). This result suggests that clusters might have formed after the Fe_3O_4-COOH NPs were modified with G5.NHAc-RGD.

The morphology and size of the G5.NHAc-Fe_3O_4 NPs and G5.NHAc-RGD-Fe_3O_4 NPs were characterized using TEM. It can be clearly observed that the Fe_3O_4-COOH NPs have a very small spherical shape and a quite uniform size distribution (Figure S2, Supporting Information). After modification, the G5.NHAc-Fe_3O_4 NPs and G5.NHAc-RGD-Fe_3O_4 NPs showed cluster structures, i.e., some interconnected particles appeared (Figure 2).

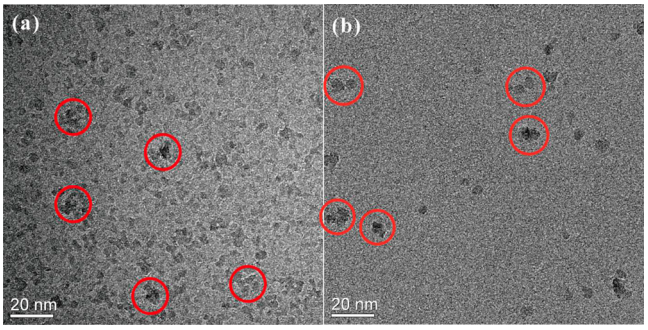

Figure 2. TEM images of G5.NHAc-Fe_3O_4 NPs (a) and G5.NHAc-RGD-Fe_3O_4 NPs (b).

The G5.NHAc-Fe_3O_4 NPs and G5.NHAc-RGD-Fe_3O_4 NPs were dispersed in different media, i.e., water, PBS, and cell culture medium, to assess their colloidal stability (Figure S3, Supporting Information). Photographs showed that the particles were stable and that no precipitates occurred in these media after 1 d.

Transverse Relaxivity (r_2) Measurement. Ultrasmall Fe_3O_4 NPs with diameters less than 5 nm have been widely used as contrast agents for T_1 MR imaging. Additionally, these particles exhibit a T_2-weighted MR imaging effect if certain clusters of particles are formed, as demonstrated in this study. The T_2 values of the water protons in an aqueous solution of G5.NHAc-RGD-Fe_3O_4 NPs and G5.NHAc-Fe_3O_4 NPs at different Fe concentrations were measured at 0.5 T, and the transverse relaxivities (r_2) of the particles were calculated based on the measured T_2 values. The results showed that the relaxation rate increased linearly with the Fe concentration for both types of particles and that the r_2 values of G5.NHAc-RGD-Fe_3O_4 NPs and G5.NHAc-Fe_3O_4 NPs were calculated to be 5.899 mM^{-1} s^{-1} and 5.425 mM^{-1} s^{-1}, respectively (Figure 3). In addition, we measured the longitudinal relaxivity (r_1) of the particles (Figure S4, Supporting Information). It can be seen that G5.NHAc-RGD-Fe_3O_4 and G5.NHAc-Fe_3O_4 NPs have r_1 values of 0.62 mM^{-1} s^{-1} and 0.66 mM^{-1} s^{-1},

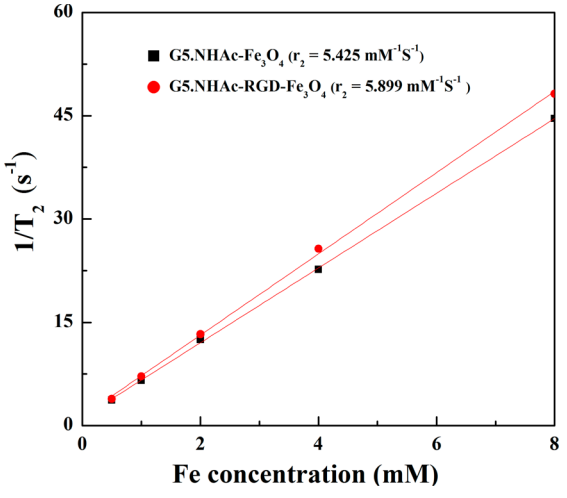

Figure 3. Linear fitting of $1/T_2$ for G5.NHAc-RGD-Fe_3O_4 NPs and G5.NHAc-Fe_3O_4 NPs with Fe concentrations of 0.5,1, 2, 4, and 8 mM.

DOI: 10.1021/am508983n
ACS Appl. Mater. Interfaces 2015, 7, 5420−5428

respectively. The large r_2/r_1 ratios (9.51 for the G5.NHAc-RGD-Fe_3O_4 NPs and 8.22 for the G5.NHAc-Fe_3O_4 NPs) suggest that these particles have excellent potential to be used as contrast agents for T_2-weighted MR imaging. The T_2-weighted images of G5.NHAc-RGD-Fe_3O_4 NPs and G5.NHAc-Fe_3O_4 NPs are shown in Figure 4. The particles induced a

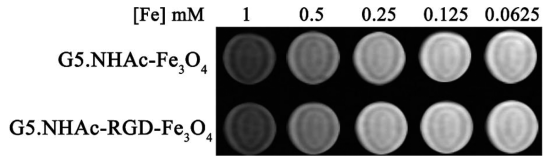

Figure 4. T_2-weighted images of G5.NHAc-RGD-Fe_3O_4 NPs and G5.NHAc-Fe_3O_4 NPs with Fe concentrations of 0.0625, 0.125, 0.25, 0.5, and 1 mM.

decrease in signal over the studied concentration range (0.0625−1 mM), indicating that the NPs synthesized in this study could be used as contrast agents for T_2 MR imaging.

Hemolysis Assay. It is very important for NPs to exhibit good hemocompatibility for use in various *in vivo* biomedical applications. The hemocompatibility of the developed G5.NHAc-RGD-Fe_3O_4 NPs and G5.NHAc-Fe_3O_4 NPs was evaluated using a hemolytic assay (Figure 5). On the basis of

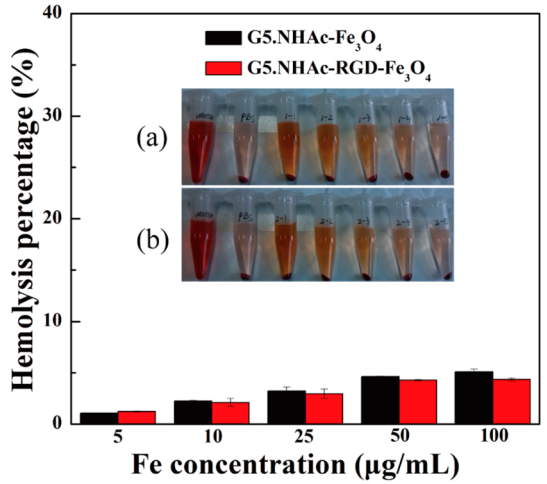

Figure 5. Hemolytic activity of G5.NHAc-Fe_3O_4 NPs (a) and G5.NHAc-RGD-Fe_3O_4 NPs (b) at different Fe concentrations (5, 10, 25, 50, and 100 μg/mL). PBS and water were used as the negative and positive controls, respectively. The middle insets show photographs of HRBCs exposed to water, PBS, and PBS containing different concentrations of NPs for 2 h followed by centrifugation.

the photographs captured, no distinct hemolysis could be observed for either particle type over the studied concentration range compared with the effects of water (positive control) or PBS (negative control). Quantitative analyses show that the hemolysis percentages of these particles were all less than 5%, even when the Fe concentration reached 100 μg/mL. Our results suggest that the G5.NHAc-RGD-Fe_3O_4 NPs and G5.NHAc-Fe_3O_4 NPs exhibit excellent hemocompatibility over the studied concentration range.

Cytotoxicity Assay and Cell Morphology Observation. Prior to implementing the nanoparticles in *in vivo* applications, it is necessary to explore the cytotoxicity of the developed G5.NHAc-RGD-Fe_3O_4 NPs and G5.NHAc-Fe_3O_4 NPs *in vitro*. After incubating C6 cells with these particles at Fe concentrations of 5, 10, 25, 50, and 100 μg/mL for 24 h, an MTT assay was performed using the standard protocol (Figure 6). No significant differences in the viabilities of the cells

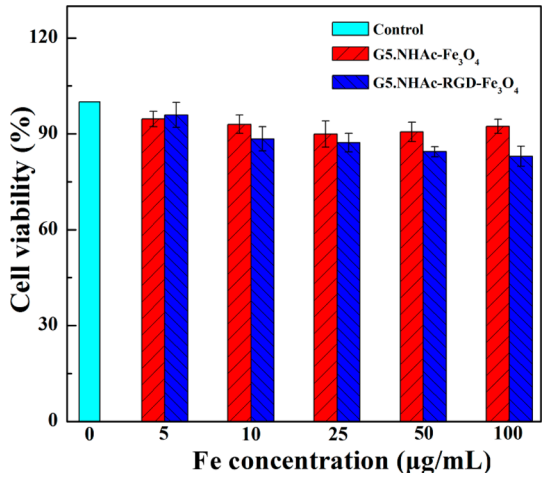

Figure 6. MTT assay of C6 cell viability after treatment with G5.NHAc-RGD-Fe_3O_4 NPs and G5.NHAc-Fe_3O_4 NPs at Fe concentrations of 0−100 μg/mL for 24 h. C6 cells treated with PBS were used as the control.

treated with the particles were observed over the studied Fe concentration range of 5−100 μg/mL compared with the viability of the PBS control. This MTT result suggests that the developed G5.NHAc-RGD-Fe_3O_4 NPs and G5.NHAc-Fe_3O_4 NPs exhibit remarkably low cytotoxicities over the given concentration range.

The morphologies of the C6 cells treated with different concentrations of G5.NHAc-RGD-Fe_3O_4 NPs and G5.NHAc-Fe_3O_4 NPs over 24 h were observed using phase contrast microscopy to further confirm the particles' lack of cytotoxicity (Figure S5, Supporting Information). All of the treated cells showed morphologies similar to those of the control cells treated with PBS, further suggesting that the G5.NHAc-RGD-Fe_3O_4 NPs and G5.NHAc-Fe_3O_4 NPs have good cytocompatibility.

Cellular Uptake Assay. ICP-AES was used to study the cellular uptake of the different particles by C6 cells (Figure 7). Concentration-dependent uptake was observed for both the G5.NHAc-RGD-Fe_3O_4 NPs and the G5.NHAc-Fe_3O_4 NPs. However, at the same Fe concentration, the uptake of the G5.NHAc-RGD-Fe_3O_4 NPs by the C6 cells was higher than that of the G5.NHAc-Fe_3O_4 NPs, particularly when the Fe concentration reached 100 μg/mL. The enhanced uptake could be due to the high affinity of G5.NHAc-RGD-Fe_3O_4 NPs for $\alpha_v\beta_3$ receptors, which are overexpressed on the surfaces of C6 cells. In sharp contrast, at the same concentration, we can clearly see that G5.NHAc-RGD-Fe_3O_4 NPs and G5.NHAc-Fe_3O_4 NPs have increased uptake by L929 cells; however, there is no obvious difference between the two different particles at similar concentrations (Figure S6, Supporting Information). It should be noted that the cellular uptake of the G5.NHAc-Fe_3O_4 NPs by C6 cells and G5.NHAc-RGD-Fe_3O_4 NPs or G5.NHAc-Fe_3O_4 NPs by L929 cells may be attributed to two distinct mechanisms (phagocytosis and diffusion through cell walls) and that the enhanced cellular uptake of G5.NHAc-RGD-Fe_3O_4 NPs by C6 cells is due to the receptor-mediated pathway.[29]

DOI: 10.1021/am508983n
ACS Appl. Mater. Interfaces 2015, 7, 5420−5428

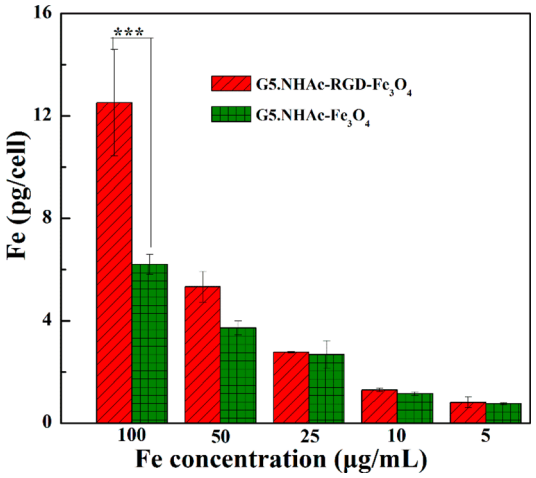

Figure 7. *In vitro* cellular uptake of G5.NHAc-RGD-Fe_3O_4 NPs and G5.NHAc-Fe_3O_4 NPs by C6 cells after treatment with different Fe concentrations for 4 h.

***In Vitro* Targeted Cell MR Imaging.** To further confirm the special ability of the G5.NHAc-RGD-Fe_3O_4 NPs to target C6 cells and to validate the particles' cell MR imaging performance, *in vitro* targeted cell MR imaging was performed. The T_2-weighted MR images of the treated cells showed a significant signal drop as a function of Fe concentration (Figure 8a). Additionally, at the same Fe concentration, the signal of

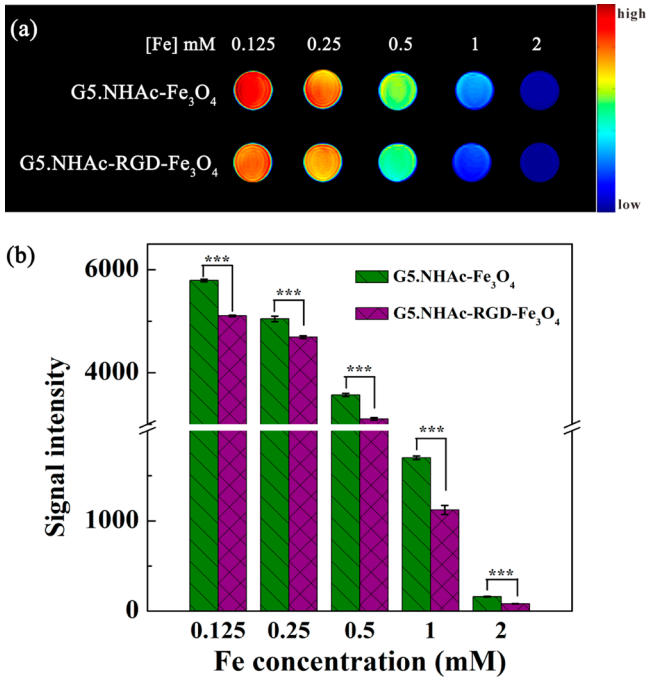

Figure 8. *In vitro* T_2-weighted MR images (a) and signal intensity (b) of C6 cells treated with G5.NHAc-RGD-Fe_3O_4 NPs and G5.NHAc-Fe_3O_4 NPs at different Fe concentrations for 4 h.

the C6 cells treated with G5.NHAc-RGD-Fe_3O_4 NPs was much lower than that of the same cells treated with G5.NHAc-Fe_3O_4 NPs. By plotting the T_2 MR signal intensity of the C6 cells treated with G5.NHAc-RGD-Fe_3O_4 NPs or G5.NHAc-Fe_3O_4 NPs as a function of Fe concentration (Figure 8b), it can be clearly observed that for both types of particles, the MR signal intensity decreases with the Fe concentration and that the signal intensity from the cells treated with G5.NHAc-RGD-Fe_3O_4 NPs is clearly lower than that of similar cells treated with G5.NHAc-Fe_3O_4 NPs at the same Fe concentration. This result further demonstrates that the modified RGD can direct the particles' targeting of C6 cells with high $\alpha_v\beta_3$ receptor expression.

***In Vivo* Targeting MR Imaging of Tumors.** The promising *in vitro* MR imaging and targeting cellular uptake results prompted an investigation into the application of G5.NHAc-RGD-Fe_3O_4 NPs for *in vivo* targeted MR imaging of C6 tumor-bearing mice. Figure 9a shows T_2-weighted MR images of a tumor obtained before injection and 0.25, 0.5, 1, and 2 h postinjection. The tumor MR signal from the mice injected with G5.NHAc-RGD-Fe_3O_4 NPs decreased from 0.25 to 0.5 h compared with the signal obtained for mice that were not injected. In contrast, no significant signal change was observed for the tumors in mice treated with G5.NHAc-Fe_3O_4 NPs during this period. One hour after injection, the MR signals of the two tumor sites were recovered, indicating that the injected particles were ejected from the tumors via a further metabolic process. The MR signal intensities from the tumors of the mice were quantitatively analyzed as a function of the postinjection time and the treatment (Figure 9b). For the targeted group, the tumor signal intensity decreased significantly from 9020 (0 h) to 4793 at 0.5 h postinjection. In contrast, only a slight decrease in MR signal intensity could be observed in the control group (mice treated with G5.NHAc-Fe_3O_4 NPs). This result suggests that in addition to the passive enhanced permeability and retention (EPR) effect, the RGD-mediated targeting pathway plays an important role in the uptake of G5.NHAc-RGD-Fe_3O_4 NPs. One hour after injection, the tumor MR signal intensity of the two groups increased due to further metabolic processes. Our results suggest that the developed G5.NHAc-RGD-Fe_3O_4 NPs have good potential for use as a tumor-targeted negative contrast agent for T_2 MR imaging.

***In Vivo* Biodistribution.** To explore the biodistribution behavior of the injected G5.NHAc-RGD-Fe_3O_4 NPs, ICP-AES was used to analyze the Fe contents in the tumor tissue and the major organs, i.e., the liver, spleen, lungs, and kidneys, at different post-treatment times (Figure 10). At 12 and 24 h, Fe was primarily taken up by the liver, spleen, and lung, and only a small amount of Fe remained in the tumor tissue and other organs, i.e., the heart and kidneys. At 48 h, the Fe content in the liver, spleen, and lung decreased due to further metabolic processes. Our results suggest that the injected G5.NHAc-RGD-Fe_3O_4 NPs can be successfully cleared from the body and will not have negative effects on animals.

CONCLUSIONS

In summary, RGD-targeted ultrasmall Fe_3O_4 NPs were developed for targeted T_2-weighted MR imaging of C6 cells *in vitro* and xenografted C6 tumors *in vivo* through a dendrimer-mediated approach. Our results indicate that the targeted NPs show good water and colloidal stability, a relaxivity (r_2) of 5.899 mM^{-1} s^{-1}, and good hemocompatibility and biocompatibility over the studied concentration range. Cellular uptake studies, *in vitro* cell MR imaging, and *in vivo* tumor imaging confirm that the developed G5.NHAc-RGD-Fe_3O_4 NPs have a high affinity for C6 cells that overexpress $\alpha_v\beta_3$ receptors. The findings obtained in this study suggest that the developed G5.NHAc-RGD-Fe_3O_4 NPs have excellent potential for use as contrast agents for targeted T_2 MR imaging of specific tumors.

DOI: 10.1021/am508983n
ACS Appl. Mater. Interfaces 2015, 7, 5420−5428

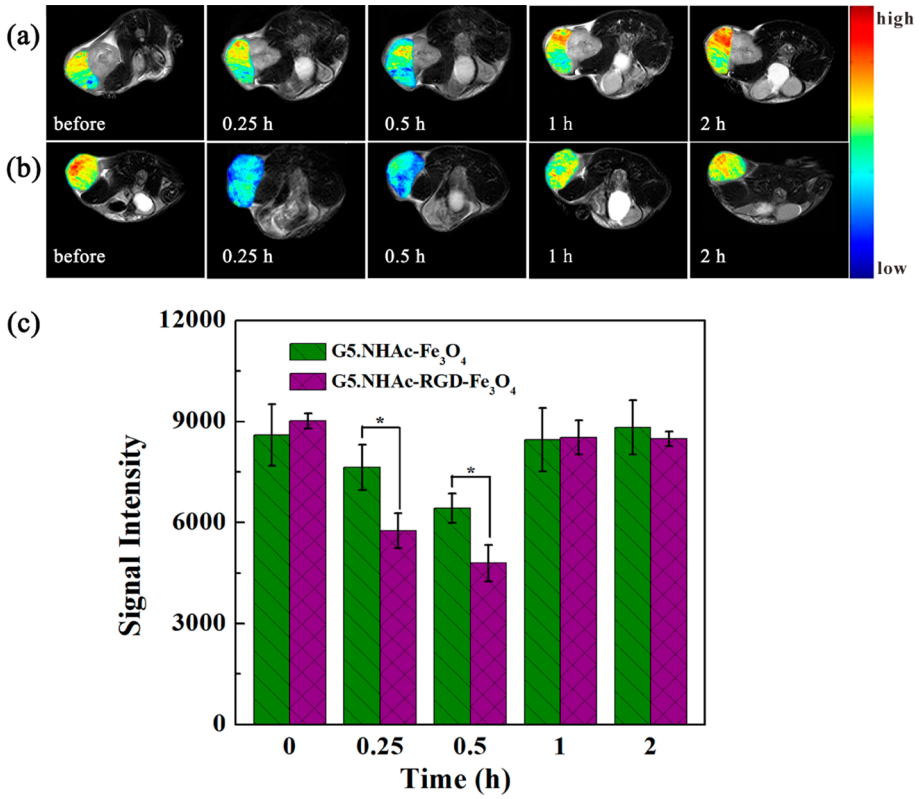

Figure 9. *In vivo* T_2-weighted MR images of tumors (a, b) and the signal intensity (c) after intravenous injections of 0.1 mL of PBS solutions containing G5.NHAc-Fe_3O_4 NPs (a) or G5.NHAc-RGD-Fe_3O_4 NPs (b) (600 μg Fe) at different times.

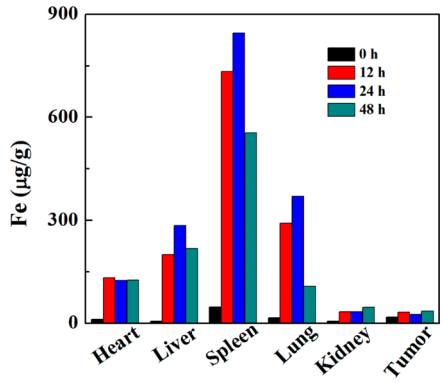

Figure 10. Biodistribution of the major organs and tissue of the mice, i.e., heart, liver, spleen, lung, kidney, and tumor, at different times post-intravenous injection of 0.1 mL of a PBS solution containing G5.NHAc-RGD-Fe_3O_4 NPs (600 μg Fe).

■ ASSOCIATED CONTENT

Supporting Information

MALDI-TOF mass spectra of G5.NH_2 and G5.NH_2-RGD dendrimers; TEM images and size distribution histogram of Fe_3O_4-COOH NPs; photographs of G5.NHAc-Fe_3O_4 NPs and G5.NHAc-RGD-Fe_3O_4 NPs dispersed in water, PBS, and culture medium; linear fitting of $1/T_1$ for the G5.NHAc-RGD-Fe_3O_4 and G5.NHAc-Fe_3O_4 NPs; phase-contrast microscopy images of C6 cells treated with PBS or G5.NHAc-Fe_3O_4 NPs; and *in vitro* cellular uptake of the G5.NHAc-RGD-Fe_3O_4 NPs and G5.NHAc-Fe_3O_4 NPs by L929 cells. This material is available free of charge via the Internet at http://pubs.acs.org.

■ AUTHOR INFORMATION

Corresponding Authors

*(X.S.) Tel: +86 21 67792656. Fax: +86 21 67792306 804. E-mail: xshi@dhu.edu.cn.

*(G.Z.) Tel: +86 21 63240090 4166. Fax: +86 21 63240825. E-mail: guixiangzhang@sina.com.

Author Contributions

‖J.Y., Y.L., and Y.X. contributed equally to this work.

Notes

The authors declare no competing financial interest.

■ ACKNOWLEDGMENTS

This research was financially supported by the National Natural Science Foundation of China (81371623, 81101150, 21273032, and 81270032) and the Fund of the Science and Technology Commission of Shanghai Municipality (11 nm0506400). We thank American Journal Experts (AJE) for their professional English language editing services.

■ REFERENCES

(1) Shi, X.; Wang, S. H.; Swanson, S. D.; Ge, S.; Cao, Z.; Van Antwerp, M. E.; Landmark, K. J.; Baker, J. R. Dendrimer-Functionalized Shell-Crosslinked Iron Oxide Nanoparticles for in Vivo Magnetic Resonance Imaging of Tumors. *Adv. Mater.* **2008**, *20*, 1671−1678.

(2) Wang, H.; Zheng, L.; Peng, C.; Shen, M.; Shi, X.; Zhang, G. Folic Acid-Modified Dendrimer-Entrapped Gold Nanoparticles as Nanoprobes for Targeted CT Imaging of Human Lung Adencarcinoma. *Biomaterials* **2013**, *34*, 470−480.

(3) Chen, Q.; Li, K.; Wen, S.; Liu, H.; Peng, C.; Cai, H.; Shen, M.; Zhang, G.; Shi, X. Targeted CT/MR Dual Mode Imaging of Tumors

DOI: 10.1021/am508983n
ACS Appl. Mater. Interfaces 2015, 7, 5420−5428

Using Multifunctional Dendrimer-Entrapped Gold Nanoparticles. *Biomaterials* **2013**, *34*, 5200−5209.
(4) Yang, M.; Cheng, K.; Qi, S.; Liu, H.; Jiang, Y.; Jiang, H.; Li, J.; Chen, K.; Zhang, H.; Cheng, Z. Affibody Modified and Radiolabeled Gold−Iron Oxide Hetero-Nanostructures for Tumor PET, Optical and MR Imaging. *Biomaterials* **2013**, *34*, 2796−2806.
(5) Huh, Y.-M.; Jun, Y.-w.; Song, H.-T.; Kim, S.; Choi, J.-s.; Lee, J.-H.; Yoon, S.; Kim, K.-S.; Shin, J.-S.; Suh, J.-S. In Vivo Magnetic Resonance Detection of Cancer by Using Multifunctional Magnetic Nanocrystals. *J. Am. Chem. Soc.* **2005**, *127*, 12387−12391.
(6) Cheon, J.; Lee, J.-H. Synergistically Integrated Nanoparticles as Multimodal Probes for Nanobiotechnology. *Acc. Chem. Res.* **2008**, *41*, 1630−1640.
(7) Zhang, W. L.; Li, N.; Huang, J.; Yu, J. H.; Wang, D. X.; Li, Y. P.; Liu, S. Y. Gadolinium-Conjugated FA-PEG-PAMAM-COOH Nanoparticles as Potential Tumor-Targeted Circulation-Prolonged Macromolecular MRI Contrast Agents. *J. Appl. Polym. Sci.* **2010**, *118*, 1805−1814.
(8) Schroeder, T. Imaging Stem-cell-driven Regeneration in Mammals. *Nature* **2008**, *453*, 345−351.
(9) Herschman, H. R. Molecular Imaging: Looking at Problems, Seeing Solutions. *Science* **2003**, *302*, 605.
(10) Zlatkin, M. B.; Chao, P. C.; Osterman, A. L.; Schnall, M. D.; Dalinka, M. K.; Kressel, H. Y. Chronic Wrist Pain: Evaluation with High-Resolution MR Imaging. *Radiology* **1989**, *173*, 723−729.
(11) Masaryk, T. J.; Ross, J. S.; Modic, M. T.; Boumphrey, F.; Bohlman, H.; Wilber, G. High-Resolution MR Imaging of Sequestered Lumbar Intervertebral Disks. *Am. J. Roentgenol.* **1988**, *150*, 1155−1162.
(12) Kim, J. H.; Beets, G. L.; Kim, M.-J.; Kessels, A. G. H.; Beets-Tan, R. G. H. High-Resolution MR Imaging for Nodal Staging in Rectal Cancer: Are There Any Criteria in Addition to the Size? *Eur. J. Radiol.* **2004**, *52*, 78−83.
(13) Wen, S.; Li, K.; Cai, H.; Chen, Q.; Shen, M.; Huang, Y.; Peng, C.; Hou, W.; Zhu, M.; Zhang, G. Multifunctional Dendrimer-Entrapped Gold Nanoparticles for Dual Mode CT/MR Imaging Applications. *Biomaterials* **2013**, *34*, 1570−1580.
(14) Swanson, S. D.; Kukowska-Latallo, J. F.; Patri, A. K.; Chen, C.; Ge, S.; Cao, Z.; Kotlyar, A.; East, A. T.; Baker, J. R. Targeted Gadolinium-Loaded Dendrimer Nanoparticles for Tumor-Specific Magnetic Resonance Contrast Enhancement. *Int. J. Nanomed.* **2008**, *3*, 201.
(15) Yang, H.; Zhuang, Y.; Sun, Y.; Dai, A.; Shi, X.; Wu, D.; Li, F.; Hu, H.; Yang, S. Targeted Dual-Contrast T_1 and T_2-weighted Magnetic Resonance Imaging of Tumors Using Multifunctional Gadolinium-Labeled Superparamagnetic Iron Oxide Nanoparticles. *Biomaterials* **2011**, *32*, 4584−4593.
(16) Chen, P.-J.; Hu, S.-H.; Hsiao, C.-S.; Chen, Y.-Y.; Liu, D.-M.; Chen, S.-Y. Multifunctional Magnetically Removable Nanogated Lids of Fe_3O_4-Capped Mesoporous Silica Nanoparticles for Intracellular Controlled Release and MR Imaging. *J. Mater. Chem.* **2011**, *21*, 2535−2543.
(17) Xie, J.; Chen, K.; Lee, H.-Y.; Xu, C.; Hsu, A. R.; Peng, S.; Chen, X.; Sun, S. Ultrasmall c (RGDyK)-Coated Fe_3O_4 Nanoparticles and Their Specific Targeting to Integrin $\alpha_v\beta_3$-rich Tumor Cells. *J. Am. Chem. Soc.* **2008**, *130*, 7542−7543.
(18) Zhang, H.; Li, J.; Sun, W.; Hu, Y.; Zhang, G.; Shen, M.; Shi, X. Hyaluronic Acid-Modified Magnetic Iron Oxide Nanoparticles for MR Imaging of Surgically Induced Endometriosis Model in Rats. *PLoS One* **2014**, *9*, e94718.
(19) Li, J.; Zheng, L.; Cai, H.; Sun, W.; Shen, M.; Zhang, G.; Shi, X. Facile One-Pot Synthesis of Fe_3O_4@Au Composite Nanoparticles for Dual-Mode MR/CT Imaging Applications. *ACS Appl. Mater. Interfaces* **2013**, *5*, 10357−10366.
(20) Ji, X.; Shao, R.; Elliott, A. M.; Stafford, R. J.; Esparza-Coss, E.; Bankson, J. A.; Liang, G.; Luo, Z.-P.; Park, K.; Markert, J. T. Bifunctional Gold Nanoshells with a Superparamagnetic Iron Oxide-Silica Core Suitable for Both MR Imaging and Photothermal Therapy. *J. Phys. Chem. C* **2007**, *111*, 6245−6251.
(21) Narayanan, S.; Sathy, B. N.; Mony, U.; Koyakutty, M.; Nair, S. V.; Menon, D. Biocompatible Magnetite/Gold Nanohybrid Contrast Agents via Green Chemistry for MRI and CT Bioimaging. *ACS Appl. Mater. Interfaces* **2011**, *4*, 251−260.
(22) Amiri, H.; Bordonali, L.; Lascialfari, A.; Wan, S.; Monopoli, M. P.; Lynch, I.; Laurent, S.; Mahmoudi, M. Protein Corona Affects the Relaxivity and MRI Contrast Efficiency of Magnetic Nanoparticles. *Nanoscale* **2013**, *5*, 8656−8665.
(23) Tschulik, K.; Compton, R. G. Nanoparticle Impacts Reveal Magnetic Field Induced Agglomeration and Reduced Dissolution Rates. *Phys. Chem. Chem. Phys.* **2014**, *16*, 13909−13913.
(24) Turcheniuk, K.; Tarasevych, A. V.; Kukhar, V. P.; Boukherroub, R.; Szunerits, S. Recent Advances in Surface Chemistry Strategies for the Fabrication of Functional Iron Oxide Based Magnetic Nanoparticles. *Nanoscale* **2013**, *5*, 10729−10752.
(25) Haubner, R.; Wester, H.-J.; Burkhart, F.; Senekowitsch-Schmidtke, R.; Weber, W.; Goodman, S. L.; Kessler, H.; Schwaiger, M. Glycosylated RGD-Containing Peptides: Tracer for Tumor Targeting and Angiogenesis Imaging with Improved Biokinetics. *J. Nucl. Med.* **2001**, *42*, 326−336.
(26) Zhou, Q.-H.; You, Y.-Z.; Wu, C.; Huang, Y.; Oupicky, D. Cyclic RGD-Targeting of Reversibly Stabilized DNA Nanoparticles Enhances Cell Uptake and Transfection in Vitro. *J. Drug Targeting* **2009**, *17*, 364−373.
(27) Garanger, E.; Boturyn, D.; Dumy, P. Tumor Targeting with RGD Peptide Ligands-Design of New Molecular Conjugates for Imaging and Therapy of Cancers. *Anti-Cancer Agents Med. Chem.* **2007**, *7*, 552−558.
(28) An, L.; Hu, H.; Du, J.; Wei, J.; Wang, L.; Yang, H.; Wu, D.; Shi, H.; Li, F.; Yang, S. Paramagnetic Hollow Silica Nanospheres for in Vivo Targeted Ultrasound and Magnetic Resonance Imaging. *Biomaterials* **2014**, *35*, 5381−5392.
(29) Li, J.; Zheng, L.; Cai, H.; Sun, W.; Shen, M.; Zhang, G.; Shi, X. Polyethyleneimine-Mediated Synthesis of Folic Acid-Targeted Iron Oxide Nanoparticles for in Vivo Tumor MR Imaging. *Biomaterials* **2013**, *34*, 8382−8392.
(30) Shi, X.; Wang, S. H.; Van Antwerp, M. E.; Chen, X.; Baker, J. R., Jr. Targeting and Detecting Cancer Cells Using Spontaneously Formed Multifunctional Dendrimer-Stabilized Gold Nanoparticles. *Analyst* **2009**, *134*, 1373−1379.
(31) Witte, L.; Hicklin, D. J.; Zhu, Z.; Pytowski, B.; Kotanides, H.; Rockwell, P.; Böhlen, P. Monoclonal Antibodies Targeting the VEGF Receptor-2 (Flk1/KDR) as an Anti-Angiogenic Therapeutic Strategy. *Cancer Metastasis Rev.* **1998**, *17*, 155−161.
(32) Cirstoiu-Hapca, A.; Bossy-Nobs, L.; Buchegger, F.; Gurny, R.; Delie, F. Differential Tumor Cell Targeting of Anti-HER2 (Herceptin) and Anti-CD20 (Mabthera) Coupled Nanoparticles. *Int. J. Phytorem.* **2007**, *331*, 190−196.
(33) Luo, K.; Liu, G.; He, B.; Wu, Y.; Gong, Q.; Song, B.; Ai, H.; Gu, Z. Multifunctional Gadolinium-Based Dendritic Macromolecules as Liver Targeting Imaging Probes. *Biomaterials* **2011**, *32*, 2575−2585.
(34) Ohya, Y.; Oue, H.; Nagatomi, K.; Ouchi, T. Design of Macromolecular Prodrug of Cisplatin Using Dextran with Branched Galactose Units as Targeting Moieties to Hepatoma Cells. *Biomacromolecules* **2001**, *2*, 927−933.
(35) Veiseh, O.; Kievit, F. M.; Fang, C.; Mu, N.; Jana, S.; Leung, M. C.; Mok, H.; Ellenbogen, R. G.; Park, J. O.; Zhang, M. Chlorotoxin Bound Magnetic Nanovector Tailored for Cancer Cell Targeting, Imaging, and siRNA Delivery. *Biomaterials* **2010**, *31*, 8032−8042.
(36) Sun, C.; Veiseh, O.; Gunn, J.; Fang, C.; Hansen, S.; Lee, D.; Sze, R.; Ellenbogen, R. G.; Olson, J.; Zhang, M. In Vivo MRI Detection of Gliomas by Chlorotoxin-Conjugated Superparamagnetic Nnanoprobes. *Small* **2008**, *4*, 372−379.
(37) Li, J.; He, Y.; Sun, W.; Luo, Y.; Cai, H.; Pan, Y.; Shen, M.; Xia, J.; Shi, X. Hyaluronic Acid-Modified Hydrothermally Synthesized Iron Oxide Nanoparticles for Targeted Tumor MR Imaging. *Biomaterials* **2014**, *35*, 3666−3677.

DOI: 10.1021/am508983n
ACS Appl. Mater. Interfaces 2015, 7, 5420−5428

(38) Lee, H.; Ahn, C.; Park, T. G. Poly [lactic-co-(glycolic acid)]-Grafted Hyaluronic Acid Copolymer Micelle Nanoparticles for Target-Specific Delivery of Doxorubicin. *Macromol. Biosci.* **2008**, *9*, 336−342.
(39) Lee, Y.; Lee, H.; Kim, Y. B.; Kim, J.; Hyeon, T.; Park, H.; Messersmith, P. B.; Park, T. G. Bioinspired Surface Immobilization of Hyaluronic Acid on Monodisperse Magnetite Nanocrystals for Targeted Cancer Imaging. *Adv. Mater.* **2008**, *20*, 4154−4157.
(40) Shen, L.-h.; Bao, J.-f.; Wang, D.; Wang, Y.-x.; Chen, Z.-w.; Ren, L.; Zhou, X.; Ke, X.-b.; Chen, M.; Yang, A.-q. One-Step Synthesis of Monodisperse, Water-Soluble Ultra-Small Fe_3O_4 Nanoparticles for Potential Bio-Application. *Nanoscale* **2013**, *5*, 2133−2141.

DOI: 10.1021/am508983n
ACS Appl. Mater. Interfaces 2015, 7, 5420−5428